

# Imaging Generalized Wigner Crystal States in a WSe<sub>2</sub>/WS<sub>2</sub> Moiré Superlattice

Feng Wang (✉ [fengwang76@berkeley.edu](mailto:fengwang76@berkeley.edu))

University of California at Berkeley <https://orcid.org/0000-0001-8369-6194>

Hongyuan Li

University of California, Berkeley <https://orcid.org/0000-0001-9119-5592>

Shaowei Li

University of California, Berkeley

Emma Regan

University of California, Berkeley

Danqing Wang

University of California, Berkeley

Wenyu Zhao

University of California, Berkeley

Salman Kahn

University of California, Berkeley <https://orcid.org/0000-0002-0012-3305>

Kentaro Yumigeta

Arizona State University

Mark Blei

Arizona State University

Takashi Taniguchi

National Institute for Materials Science, Tsukuba, Ibaraki <https://orcid.org/0000-0002-1467-3105>

Kenji Watanabe

National Institute for Materials Science <https://orcid.org/0000-0003-3701-8119>

Sefaattin Tongay

Arizona State University

Alex Zettl

University of California, Berkeley

Michael Crommie

University of California, Berkeley <https://orcid.org/0000-0001-8246-3444>

---

Physical Sciences - Article

**Keywords:** Wigner crystal state, condensed matter physics

**Posted Date:** April 7th, 2021

**DOI:** <https://doi.org/10.21203/rs.3.rs-390032/v1>

**License:**  This work is licensed under a Creative Commons Attribution 4.0 International License.

[Read Full License](#)

---

**Version of Record:** A version of this preprint was published at Nature on September 29th, 2021. See the published version at <https://doi.org/10.1038/s41586-021-03874-9>.

## Abstract

The Wigner crystal state, first predicted by Eugene Wigner in 1934<sup>1</sup>, has fascinated condensed matter physicists for nearly 90 years<sup>2-10</sup>. Studies of two-dimensional (2D) electron gases first revealed signatures of the Wigner crystal in electrical transport measurements at high magnetic fields<sup>2-4</sup>. More recently optical spectroscopy has provided evidence of generalized Wigner crystal states in transition metal dichalcogenide (TMDC) moiré superlattices<sup>6-9</sup>. Direct observation of the 2D Wigner crystal lattice in real space, however, has remained an outstanding challenge. Scanning tunneling microscopy (STM) in principle has sufficient spatial resolution to image the Wigner crystal, but conventional STM measurements can potentially alter fragile Wigner crystal states in the process of measurement. Here we demonstrate real-space imaging of 2D Wigner crystals in WSe<sub>2</sub>/WS<sub>2</sub> moiré heterostructures using a novel non-invasive STM spectroscopy technique. We employ a graphene sensing layer in close proximity to the WSe<sub>2</sub>/WS<sub>2</sub> moiré superlattice for Wigner crystal imaging, where local STM tunneling current into the graphene sensing layer is modulated by the underlying electron lattice of the Wigner crystal in the WSe<sub>2</sub>/WS<sub>2</sub> heterostructure. Our measurement directly visualizes different lattice configurations associated with Wigner crystal states at fractional electron fillings of  $n = 1/3, 1/2$ , and  $2/3$ , where  $n$  is the electron number per site. The  $n=1/3$  and  $n=2/3$  Wigner crystals are observed to exhibit a triangle and a honeycomb lattice, respectively, in order to minimize nearest-neighbor occupations. The  $n = 1/2$  state, on the other hand, spontaneously breaks the original C3 symmetry and forms a stripe structure in real space. Our study lays a solid foundation toward the fundamental understanding of rich Wigner crystal states in WSe<sub>2</sub>/WS<sub>2</sub> moiré heterostructures. Furthermore, this new STM technique is generally applicable to imaging novel correlated electron lattices in different van der Waals moiré heterostructures.

## Main Text

A Wigner crystal is the crystalline phase of electrons stabilized at low electron density, where long-range Coulomb interactions dominate over quantum fluctuations in electron motion. The long pursuit of Wigner crystals<sup>2-10</sup> has motivated the study of 2D electron gases at high magnetic field where electron kinetic energy is quenched by degenerate Landau levels<sup>11, 12</sup> and has led to the discovery of new quantum hall states<sup>13, 14</sup>. Electrical transport signatures of Wigner crystal states have been reported in extremely clean GaAs/AlGaAs quantum wells<sup>2, 3</sup> as well as graphene<sup>4</sup> at sufficiently low doping and high magnetic field. Recently, the discovery of moiré flat minibands in van der Waals heterostructures has opened a new route to realize Wigner crystal states at zero magnetic field. Several optical and conductance measurements have provided evidence of rich generalized Wigner crystal states in different TMDC moiré superlattices<sup>6-9</sup>. However, the direct observation of the real-space electron lattice in 2D, however, has remained challenging experimentally.

Real-space imaging of 2D Wigner crystals requires a measurement technique that satisfies several stringent requirements. It must (1) have sufficient spatial resolution to resolve the electron lattice, (2) have sufficient sensitivity to detect the presence of single electrons in the lattice, (3) be adequately non-

invasive to not destroy the fragile Wigner crystal states. The last two requirements conflict with each other since strong coupling to the Wigner crystal is required for high sensitivity, whereas weak coupling is required to avoid strongly perturbing fragile states. For example, conventional STM measurements have excellent spatial resolution and charge sensitivity but can be highly invasive since inevitable tip-gating effects at finite tip bias can destroy the delicate electron lattice of the Wigner crystal. In this work, we utilize a novel STM measurement scheme that strikes a balance between these two contradictory requirements, thus enabling real-space imaging of the  $n=2/3$ ,  $n=1/2$ , and  $n=1/3$  2D Wigner crystal states in  $\text{WSe}_2/\text{WS}_2$  moiré heterostructures.

Our new STM scheme employs a specially designed van der Waals heterostructure as illustrated in Fig. 1a (see Methods for the sample fabrication details). It integrates a gated  $\text{WSe}_2/\text{WS}_2$  moiré heterostructure and a top graphene monolayer sensing layer that are separated by a hexagonal boron nitride (hBN) layer with a thickness  $d_t = 5\text{nm}$ , chosen to be smaller than the moiré lattice constant ( $L_M = 8\text{nm}$ ). This separation is small enough that the STM tip and graphene sensing layer can efficiently couple to individual moiré electrons in the  $\text{WSe}_2/\text{WS}_2$  superlattice, but it is large enough that the tip and graphene layer remain non-invasive with respect to the delicate Wigner crystal states. STM tunneling current into the graphene sensing layer can be modulated by the charge states of different moiré sites in the  $\text{WSe}_2/\text{WS}_2$  superlattice through local Coulomb blockade effects<sup>15</sup>. This technique allows us to detect the local charge distribution in the  $\text{WSe}_2/\text{WS}_2$  heterostructure and to image the embedded Wigner crystal lattice.

Fig. 1b shows a typical large-scale topography image measured on the top graphene surface. The top graphene and hBN layers cover the  $\text{WSe}_2/\text{WS}_2$  heterostructure conformally and inherit the topography of the 3D reconstructed moiré superlattice<sup>16</sup> below. Fig. 1c shows a zoom-in topographic image corresponding to the red dashed box area in Fig. 1b. A red rhombus labels the primitive cell of the moiré superlattice with the high points corresponding to AA stacking regions and the two inequivalent low points corresponding to distinct AB stacking regions (denoted  $\text{AB}_1$  and  $\text{AB}_2$ )<sup>16</sup>. The moiré lattice constant  $L_M = 8\text{nm}$  indicates a near-0° twist angle between the  $\text{WSe}_2$  and  $\text{WS}_2$  layers.

We implement dual gates in our van der Waals heterostructure devices (Fig. 1a), with the top monolayer graphene acting as both sensing layer and top gate and the silicon substrate acting as back gate. The top gate dielectric is defined by the top hBN flake ( $d_t = 5\text{nm}$ ) while the bottom gate dielectric is defined by a combination of  $\text{SiO}_2$  ( $d_{\text{SiO}_2} = 285\text{nm}$ ) and hBN ( $d_b = 70\text{nm}$ ). The carrier densities in the TMDC moiré heterostructure and the top graphene can be controlled independently via the top gate voltage,  $V_{TG}$ , and bottom gate voltage,  $V_{BG}$ . In this study we mainly focus on the electron-doped regime of the  $\text{WSe}_2/\text{WS}_2$  heterostructure.

For  $V_{TG} = 0$ , the Fermi level is within the band gap of the  $\text{WSe}_2/\text{WS}_2$  heterostructure (see illustration in Fig. 1d). In this case, tuning  $V_{BG}$  dopes charge carriers exclusively into the graphene layer. Fig. 1e shows the  $V_{BG}$  dependent STM differential conductivity ( $dI/dV$ ) spectra of graphene measured at  $V_{TG} = 0$ . The

dispersive feature labeled by the white dashed line shows the evolution of the graphene charge neutral point (CNP) in response to the electrostatic doping from  $V_{BG}$ <sup>17-19</sup>. The persistent gap near  $V_{bias} = 0$  arises from an inelastic tunneling gap that occurs at all gate voltages. This inelastic tunneling gap causes the graphene CNP curve to abruptly shift as it shifts over the zero-bias region<sup>17, 19</sup>.

We are able to dope electrons into the WSe<sub>2</sub>/WS<sub>2</sub> heterostructure by applying a positive  $V_{TG}$  such that the Fermi level of the WSe<sub>2</sub>/WS<sub>2</sub> heterostructure lies near the conduction band edge (see illustration in Fig. 1f). Here we choose  $V_{TG} \sim 0.5V$  so that the WSe<sub>2</sub>/WS<sub>2</sub> heterostructure can be electron doped while the graphene sensing layer remains close to charge neutral. This configuration provides the highest sensitivity for imaging Wigner crystal states in the moiré superlattice. Fig. 1g show the resulting  $dI/dV$  tunneling spectra into the graphene sensing layer as a function of  $V_{BG}$  at a fixed  $V_{TG} = 0.53V$ . This panel shows a zoom-in view of the electron-doped regime, corresponding to the phase space outlined by the white dashed box in Fig.1e.

Fig. 1g shows that the graphene is hole-doped at  $V_{BG} < 7V$ , because it is impossible to inject holes into the WSe<sub>2</sub>/WS<sub>2</sub> heterostructure with the band alignment shown in Fig. 1f. This hole doping leads to dispersive movement of the graphene CNP at  $V_{BG} < 7V$  (denoted by the white dashed line in Fig. 1g). Electron doping at  $V_{BG} > 7V$ , however, behaves rather differently. In a non-interacting single particle picture, the electron doping occurs predominantly in the WSe<sub>2</sub>/WS<sub>2</sub> heterostructure because its density of state (DOS) is orders of magnitude larger than the graphene DOS at the Dirac point. Therefore one would expect the graphene Fermi energy to be fixed near the Dirac point, as illustrated by the vertical dashed line at  $V_{BG} > 7V$ . Experimentally, however, we observe a non-trivial shift of the Fermi energy in graphene at different electron densities. Electron doping of the graphene layer takes place when the WSe<sub>2</sub>/WS<sub>2</sub> heterostructure experiences fractional filling of the moiré superlattice with  $n=1/3, 1/2, 2/3$ , and  $1$  (black dashed lines in Fig. 1g). Figure 1h shows a vertical line-cut of the gate-dependent  $dI/dV$  spectra at  $V_{bias} = 0.1V$ , which shows clear peaks at these fractional fillings. These features signify the correlated gaps in the WSe<sub>2</sub>/WS<sub>2</sub> Mott insulator state at  $n=1$  as well as the generalized Wigner crystal insulator states at  $n=1/3, 1/2, 2/3$ . This is due to the fact that the correlated gaps make the WSe<sub>2</sub>/WS<sub>2</sub> heterostructure electronically incompressible and so electrons are electrostatically forced into the graphene sensing layer. Similar effects have been observed in capacitance and single-electron-transistor measurements of the electronic compressibility in different van der Waals heterostructure systems<sup>20-24</sup>. Our STM configuration thus provides a new technique for mapping the local electronic compressibility of correlated insulating states in moiré superlattices.

Real-space imaging of the 2D electron lattice of the Mott insulator and Wigner crystal states is performed through 2D  $dI/dV$  mapping of the graphene sensing layer, as illustrated in the measurement scheme of Fig. 2a. The Mott and Wigner crystal states form periodic electron lattices in the WSe<sub>2</sub>/WS<sub>2</sub> moiré heterostructure that couple to the graphene sensing layer and STM tip through long-range Coulomb interactions. The tunnel current between the STM tip and the graphene layer will vary spatially depending

on the charge state of the WSe<sub>2</sub>/WS<sub>2</sub> moiré site below the STM tip. As a result, the electron lattices of the Mott and Wigner crystal states can be imaged as periodic lattice structures in 2D dI/dV mappings of the graphene sensing layer.

Fig. 2b displays the topographic image of a typical region of the WSe<sub>2</sub>/WS<sub>2</sub> moiré superlattice as seen by scanning the top graphene layer. Here we marked the triangular lattice formed by the AB<sub>1</sub> stacking sites with solid red dots. This region exhibits a lattice that is free of distortion or atomic defects, an essential condition for observing Mott and Wigner crystal states with long-range order.

Fig. 2c shows the 2D dI/dV mapping of the graphene layer when the WSe<sub>2</sub>/WS<sub>2</sub> moiré heterostructure is in the n = 1 Mott insulator state ( $V_{\text{bias}} = 160\text{mV}$ ,  $V_{\text{BG}} = 30\text{V}$ , and  $V_{\text{TG}} = 0.53\text{ V}$ ; see Methods for more measurement details). A highly ordered triangular lattice of bright dots can be clearly observed that corresponds closely to the AB<sub>1</sub> stacking sites of the moiré superlattice. Such AB<sub>1</sub> stacking sites are illustrated as red dots in Fig. 2b. Since the AB<sub>1</sub> and AB<sub>2</sub> stackings sites are similar in topography, the localization of the bright features in Fig. 1c at the AB<sub>1</sub> stacking sites implies that they do not originate from topography, but rather from the underlying electron lattice of the Mott insulator state. This is consistent with previous work showing that conduction flat band electrons in the WSe<sub>2</sub>/WS<sub>2</sub> moiré heterostructure are localized at one of the AB stacking sites<sup>15</sup>. Fig. 2d displays the fast Fourier transform (FFT) image of the dI/dV map in Fig. 2c, showing sharp diffraction points associated with the electron lattice of the Mott insulator state. The reciprocal unit vectors of the moiré superlattice are marked by green dots in the FFT images and are seen to overlap perfectly with the lowest order diffraction points of the Mott insulator electron lattice.

We next image the generalized Wigner crystal states at fractional fillings. Fig. 2e shows the dI/dV mapping of the n = 2/3 generalized Wigner crystal state ( $V_{\text{bias}} = 160\text{mV}$ ,  $V_{\text{BG}} = 21.8\text{V}$ ,  $V_{\text{TG}} = 0.458\text{ V}$ ). FFT filtering has been performed in the Wigner crystal images (Fig. 2e-2j) to suppress the periodic features associated with the moiré superlattice (i.e. green dots in Fig. 2f. See SI for unfiltered images). The n = 2/3 dI/dV map exhibits a honeycomb lattice with lattice constant . This is consistent with 2/3 of the available AB<sub>1</sub> sites being filled with electrons (solid red dots) and the other 1/3 AB<sub>1</sub> sites being empty (open red circles) so as to minimize total nearest-neighbor interactions. Such a honeycomb lattice matches well with previous predictions<sup>6-9</sup>, and demonstrates the existence of the generalized Wigner crystal states, where moiré electrons are stabilized by long-range Coulomb interactions and exhibit well-defined 2D crystalline order. The corresponding FFT image (Fig. 2f) confirms the emergence of a new lattice: six sharp diffraction points associated with the generalized Wigner crystal lattice appear inside the reciprocal unit vectors (green dots) of moiré superlattice.

Figs. 2g and 2h show the dI/dV map and corresponding FFT image, respectively, of the n=1/3 generalized Wigner crystal state. The real-space image demonstrates a new triangular electron lattice associated with the Wigner crystal state where 1/3 of the available AB<sub>1</sub> sites are filled with electrons (solid red dots) and the other 2/3 AB<sub>1</sub> sites are empty (open red circles). The FFT image shows a clear diffraction pattern of

the generalized Wigner crystal state with a lattice constant of . We note that the diffraction pattern of the  $n = 2/3$  and  $n = 1/3$  states are nearly identical because both states share the same primitive cell and are linked by a particle-hole transformation.

Fig. 2i shows 2D  $dI/dV$  map of the  $n = 1/2$  generalized Wigner crystal state with  $V_{bias} = 125\text{mV}$ ,  $V_{BG} = 18.7\text{V}$ , and  $V_{TG} = 0.458 \text{ V}$ . It reveals unambiguously that the C3 symmetry of the host moiré superlattice is spontaneously broken for this generalized Wigner crystal state. The  $n = 1/2$  state features a stripe symmetry with electrons (solid red dots) filling the  $AB_1$  sites in alternating lines (empty sites are denoted by open red circles). The lattice constants of this stripe phase are and along the parallel and perpendicular directions, respectively. The corresponding FFT image in Fig. 2j shows rhombus-like reciprocal unit vectors, further confirming the broken symmetry of the stripe phase for the  $n = 1/2$  generalized Wigner crystal state.

The  $n=1/2$  generalized Wigner crystal state is predicted to be highly degenerate, with multiple electron lattice configurations having the same energy in the case of only nearest-neighbor interactions<sup>7</sup>. The spontaneous broken symmetry of the  $n = 1/2$  state might then be governed by higher-order effects, such as next-nearest-neighbor interactions and/or accidental strain in the lattice. Experimentally we here found that the  $n = 1/2$  state is more fragile than the  $n=1/3$  and  $n=2/3$  states. A well-defined generalized Wigner crystal stripe phase is present only in a very narrow parameter space of  $V_{bias}$  and  $V_{BG}$ . In addition, the  $n = 1/2$  state is more sensitive to local inhomogeneity, as reflected by the disordering of the stripe electron lattice near the right edge of the image in Fig. 2i, compared with the  $n=2/3$  (Fig. 2c) and  $n=1/3$  (Fig. 2e) states. Further studies of the generalized Wigner crystal electron lattice at  $n = 1/2$  could potentially lead to a better understanding of the competition of different quantum phases controlled by long-range Coulomb interactions.

We last discuss the imaging mechanism underlying the 2D  $dI/dV$  mapping of generalized Wigner crystal electron lattices in the presence of a graphene sensing layer. As illustrated in Fig. 2a, the STM tunneling current into the graphene layer can be coupled to the moiré electron below the tip through the long-range Coulomb interaction. This coupling can affect the tunnel current in two different ways: (1) The localized moiré electron can induce local band bending in the graphene sensing layer, thus changing the graphene local density of states and hence the  $dI/dV$  signal. (2) Application of  $V_{bias}$  can induce local band bending in the  $\text{WSe}_2/\text{WS}_2$  moiré superlattice under the tip, thus discharging the moiré electron below the tip once  $V_{bias}$  exceeds a threshold value. This mechanism is helped by the fact that electrical screening by the top monolayer graphene is weak when its Fermi level is close to the Dirac point. A resulting moiré electron discharging event then leads to a sudden increase in the STM tunneling current due to the elimination of the Coulomb blockade effect, hence contributing to the  $dI/dV$  signal<sup>15</sup>.

To distinguish between these two mechanisms we have systematically examined how the 2D  $dI/dV$  maps evolve as  $V_{bias}$  is changed. Figs. 3a-e show the  $dI/dV$  maps of the  $n = 2/3$  Wigner crystal state as  $V_{bias}$  is increased from 130mV to 190mV in 15mV steps. No FFT filtering was performed on these

images. The honeycomb electron lattice associated with the  $n = 2/3$  generalized Wigner crystal state is not clearly seen in the  $dI/dV$  map at  $V_{bias} = 130$  mV (Fig. 3a), but emerges when  $V_{bias}$  is increased to 145 mV (Fig. 3b). The dominant features are the bright dots centered on the  $AB_1$  stacking sites. These features expand with increased  $V_{bias}$  (Fig. 3c) and ultimately form ring-like features (Figs. 3d,e). Such behavior (i.e. expanding rings with increased tip bias) is characteristic of tip-induced electrical discharging rings<sup>15, 25-28</sup>, which occurs because electrical discharging for larger distant tip-electron distances requires larger tip biases. This indicates that mechanism (2) discussed above is the dominant contrast mechanism for imaging Wigner crystal states in our  $dI/dV$  maps. The STM tip locally discharges the moiré electron localized at the  $AB_1$  site closest to the tip apex once  $V_{bias}$  is large enough and the tip-electron distance is short enough. This enables discharge features centered around *filled*  $AB_1$  sites to be observed in  $dI/dV$  maps of the graphene sensing layer.

In conclusion, we have developed a new STM imaging technique that combines high spatial resolution and sensitivity with minimal perturbation to the probed electronic system. This technique has enabled us to directly image the delicate 2D electron lattices of generalized Wigner crystals in real space. Our technique should be generally applicable to a wide variety of van der Waals moiré heterostructure and provides a powerful new tool for imaging real-space electron configurations of novel correlated quantum phases in 2D systems.

## Methods

**Sample fabrication:** The encapsulated  $WSe_2/WS_2$  moire heterostructure stack was fabricated using the micro-mechanical stacking technique. A poly(propylene) carbonate (PPC) film stamp was used to pick up all exfoliated 2D material flakes. The 2D material layers in the main heterostructure region were picked up in the following order: bottom hBN,  $WSe_2$ ,  $WS_2$ , top hBN, and then monolayer graphene. A graphite layer was also picked up between the  $WS_2$  and the top hBN to serve as a contact electrode of the  $WSe_2/WS_2$  heterostructure. The PPC film together with the stacked sample was then peeled, flipped over, and transferred onto a Si/SiO<sub>2</sub> substrate (SiO<sub>2</sub> thickness 285nm). The PPC layer was subsequently removed using ultrahigh vacuum annealing at 230 °C, resulting in an atomically-clean heterostructure suitable for STM measurements. A 50nm Au and 5nm Cr metal layer was evaporated through a shadow mask to form the electric contact at the end.

**$dI/dV$  mapping:** A modulation of 15mV amplitude and 500~900 Hz frequency was applied to the tip bias to obtain the  $dI/dV$  signal. The  $dI/dV$  mapping of the Mott-insulator state in Fig. 2c was performed under the open-loop conditions, where the tip height was set by the parameters:  $V_{bias} = 180$ mV and  $I = 300$  pA. The  $dI/dV$  mappings of the generalized Wigner crystals states were performed under the constant-bias mode if not further specified.

## Declarations

## Corresponding Author

\* Email: [swli@berkeley.edu](mailto:swli@berkeley.edu) (S.L.), [crommie@physics.berkeley.edu](mailto:crommie@physics.berkeley.edu) (M.C.) and [fengwang76@berkeley.edu](mailto:fengwang76@berkeley.edu) (F.W.).

## Author Contributions

M.C. and F.W. conceived the project. H.L., S.L. performed the STM measurement, H.L., E.R., D.W., W.Z., and S.K. fabricated the heterostructure device and performed the SHG measurement. K.Y., M.B. and S.T. grew WSe<sub>2</sub> and WS<sub>2</sub> crystals. K.W. and T.T. grew the hBN single crystal. All authors discussed the results and wrote the manuscript.

## Notes

The authors declare no financial competing interests.

## ACKNOWLEDGMENT

This work was primarily funded by the U.S. Department of Energy, Office of Science, Office of Basic Energy Sciences, Materials Sciences and Engineering Division under Contract No. DE-AC02-05-CH11231 (van der Waals heterostructure program KCFW16) (device electrode preparation and STM spectroscopy). Support was also provided by the US Army Research Office under MURI award W911NF-17-1-0312 (device layer transfer), and by the National Science Foundation Award DMR-1807233 (surface preparation). S.T acknowledges support from DOE-SC0020653, NSF DMR 2111812, NSF DMR 1552220, NSF 2052527, DMR 1904716, and NSF CMMI 1933214 for WSe<sub>2</sub> and WS<sub>2</sub> bulk crystal growth and analysis. K.W. and T.T. acknowledge support from the Elemental Strategy Initiative conducted by the MEXT, Japan, Grant Number JPMXP0112101001, JSPS KAKENHI Grant Number JP20H00354 and the CREST(JPMJCR15F3), JST for bulk hBN crystal growth and analysis. E.C.R. acknowledges support from the Department of Defense (DoD) through the National Defense Science & Engineering Graduate Fellowship (NDSEG) Program. S.L. acknowledges support from Kavli ENSI Heising Simons Junior Fellowship.

## Supplementary Materials

## Data availability

The data supporting the findings of this study are included in the main text and in the Supplementary Information files, and are also available from the corresponding authors upon reasonable request.

## References

1. Wigner, E. *On the interaction of electrons in metals*. *Physical Review* **1934**, *46*, (11), 1002.
2. Goldman, V.; Santos, M.; Shayegan, M.; Cunningham, J. *Evidence for two-dimentional quantum Wigner crystal*. *Physical review letters* **1990**, *65*, (17), 2189.

3. Jang, J.; Hunt, B. M.; Pfeiffer, L. N.; West, K. W.; Ashoori, R. C. *Sharp tunnelling resonance from the vibrations of an electronic Wigner crystal*. *Nature Physics* **2017**, *13*, (4), 340-344.
4. Zhou, H.; Polshyn, H.; Taniguchi, T.; Watanabe, K.; Young, A. *Solids of quantum Hall skyrmions in graphene*. *Nature Physics* **2020**, *16*, (2), 154-158.
5. Shapir, I.; Hamo, A.; Pecker, S.; Moca, C.; Legeza, Ö.; Zarand, G.; Ilani, S. *Imaging the electronic Wigner crystal in one dimension*. *Science* **2019**, *364*, (6443), 870-875.
6. Regan, E. C.; Wang, D.; Jin, C.; Utama, M. I. B.; Gao, B.; Wei, X.; Zhao, S.; Zhao, W.; Zhang, Z.; Yumigeta, K. *Mott and generalized Wigner crystal states in WSe<sub>2</sub>/WS<sub>2</sub> moiré superlattices*. *Nature* **2020**, *579*, (7799), 359-363.
7. Jin, C.; Tao, Z.; Li, T.; Xu, Y.; Tang, Y.; Zhu, J.; Liu, S.; Watanabe, K.; Taniguchi, T.; Hone, J. C. *Stripe phases in WSe<sub>2</sub>/WS<sub>2</sub> moiré superlattices*. *arXiv preprint arXiv:2007.12068* **2020**.
8. Xu, Y.; Liu, S.; Rhodes, D. A.; Watanabe, K.; Taniguchi, T.; Hone, J.; Elser, V.; Mak, K. F.; Shan, J. *Correlated insulating states at fractional fillings of moiré superlattices*. *Nature* **2020**, *587*, (7833), 214-218.
9. Huang, X.; Wang, T.; Miao, S.; Wang, C.; Li, Z.; Lian, Z.; Taniguchi, T.; Watanabe, K.; Okamoto, S.; Xiao, D. *Correlated insulating states at fractional fillings of the WS<sub>2</sub>/WSe<sub>2</sub> moiré lattice*. *Nature Physics* **2021**, 1-5.
10. Deshpande, V. V.; Bockrath, M. *The one-dimensional Wigner crystal in carbon nanotubes*. *Nature Physics* **2008**, *4*, (4), 314-318.
11. Lam, P. K.; Girvin, S. *Liquid-solid transition and the fractional quantum-Hall effect*. *Physical Review B* **1984**, *30*, (1), 473.
12. Levesque, D.; Weis, J.; MacDonald, A. *Crystallization of the incompressible quantum-fluid state of a two-dimensional electron gas in a strong magnetic field*. *Physical Review B* **1984**, *30*, (2), 1056.
13. Tsui, D. C.; Stormer, H. L.; Gossard, A. C. *Two-dimensional magnetotransport in the extreme quantum limit*. *Physical Review Letters* **1982**, *48*, (22), 1559.
14. Klitzing, K. v.; Dorda, G.; Pepper, M. *New method for high-accuracy determination of the fine-structure constant based on quantized Hall resistance*. *Physical review letters* **1980**, *45*, (6), 494.
15. Li, H.; Li, S.; Naik, M. H.; Xie, J.; Li, X.; Regan, E.; Wang, D.; Zhao, W.; Yumigeta, K.; Blei, M. *Imaging local discharge cascades for correlated electrons in WS<sub>2</sub>/WSe<sub>2</sub> moiré superlattices*. *arXiv preprint arXiv:2102.09986* **2021**.
16. Li, H.; Li, S.; Naik, M. H.; Xie, J.; Li, X.; Wang, J.; Regan, E.; Wang, D.; Zhao, W.; Zhao, S. *Imaging moiré flat bands in three-dimensional reconstructed WSe<sub>2</sub>/WS<sub>2</sub> superlattices*. *Nature Materials* **2021**, 1-6.
17. Zhang, Y.; Brar, V. W.; Wang, F.; Girit, C.; Yayon, Y.; Panlasigui, M.; Zettl, A.; Crommie, M. F. *Giant phonon-induced conductance in scanning tunnelling spectroscopy of gate-tunable graphene*. *Nature Physics* **2008**, *4*, (8), 627-630.
18. Jung, S.; Rutter, G. M.; Klimov, N. N.; Newell, D. B.; Calizo, I.; Hight-Walker, A. R.; Zhitenev, N. B.; Stroscio, J. A. *Evolution of microscopic localization in graphene in a magnetic field from scattering*

resonances to quantum dots. *Nature Physics* **2011**, *7*, (3), 245-251.

19. Decker, R.; Wang, Y.; Brar, V. W.; Regan, W.; Tsai, H.-Z.; Wu, Q.; Gannett, W.; Zettl, A.; Crommie, M. F. *Local electronic properties of graphene on a BN substrate via scanning tunneling microscopy. Nano letters* **2011**, *11*, (6), 2291-2295.
20. Yang, F.; Zibrov, A. A.; Bai, R.; Taniguchi, T.; Watanabe, K.; Zaletel, M. P.; Young, A. F. *Experimental determination of the energy per particle in partially filled Landau levels. arXiv preprint arXiv:2008.05466* **2020**.
21. Li, T.; Zhu, J.; Tang, Y.; Watanabe, K.; Taniguchi, T.; Elser, V.; Shan, J.; Mak, K. F. *Charge-order-enhanced capacitance in semiconductor moiré superlattices. arXiv preprint arXiv:2102.10823* **2021**.
22. Tomarken, S. L.; Cao, Y.; Demir, A.; Watanabe, K.; Taniguchi, T.; Jarillo-Herrero, P.; Ashoori, R. *Electronic compressibility of magic-angle graphene superlattices. Physical review letters* **2019**, *123*, (4), 046601.
23. Zondiner, U.; Rozen, A.; Rodan-Legrain, D.; Cao, Y.; Queiroz, R.; Taniguchi, T.; Watanabe, K.; Oreg, Y.; von Oppen, F.; Stern, A. *Cascade of phase transitions and Dirac revivals in magic-angle graphene. Nature* **2020**, *582*, (7811), 203-208.
24. Pierce, A. T.; Xie, Y.; Park, J. M.; Khalaf, E.; Lee, S. H.; Cao, Y.; Parker, D. E.; Forrester, P. R.; Chen, S.; Watanabe, K. *Unconventional sequence of correlated Chern insulators in magic-angle twisted bilayer graphene. arXiv preprint arXiv:2101.04123* **2021**.
25. Pradhan, N. A.; Liu, N.; Silien, C.; Ho, W. *Atomic scale conductance induced by single impurity charging. Physical review letters* **2005**, *94*, (7), 076801.
26. Brar, V. W.; Decker, R.; Solowan, H.-M.; Wang, Y.; Maserati, L.; Chan, K. T.; Lee, H.; Girit, Ç. O.; Zettl, A.; Louie, S. G. *Gate-controlled ionization and screening of cobalt adatoms on a graphene surface. Nature Physics* **2011**, *7*, (1), 43-47.
27. Wong, D.; Velasco, J.; Ju, L.; Lee, J.; Kahn, S.; Tsai, H.-Z.; Germany, C.; Taniguchi, T.; Watanabe, K.; Zettl, A. *Characterization and manipulation of individual defects in insulating hexagonal boron nitride using scanning tunnelling microscopy. Nature nanotechnology* **2015**, *10*, (11), 949-953.
28. Teichmann, K.; Wenderoth, M.; Loth, S.; Ulbrich, R.; Garleff, J.; Wijnheijmer, A.; Koenraad, P. *Controlled charge switching on a single donor with a scanning tunneling microscope. Physical review letters* **2008**, *101*, (7), 076103.

## Figures

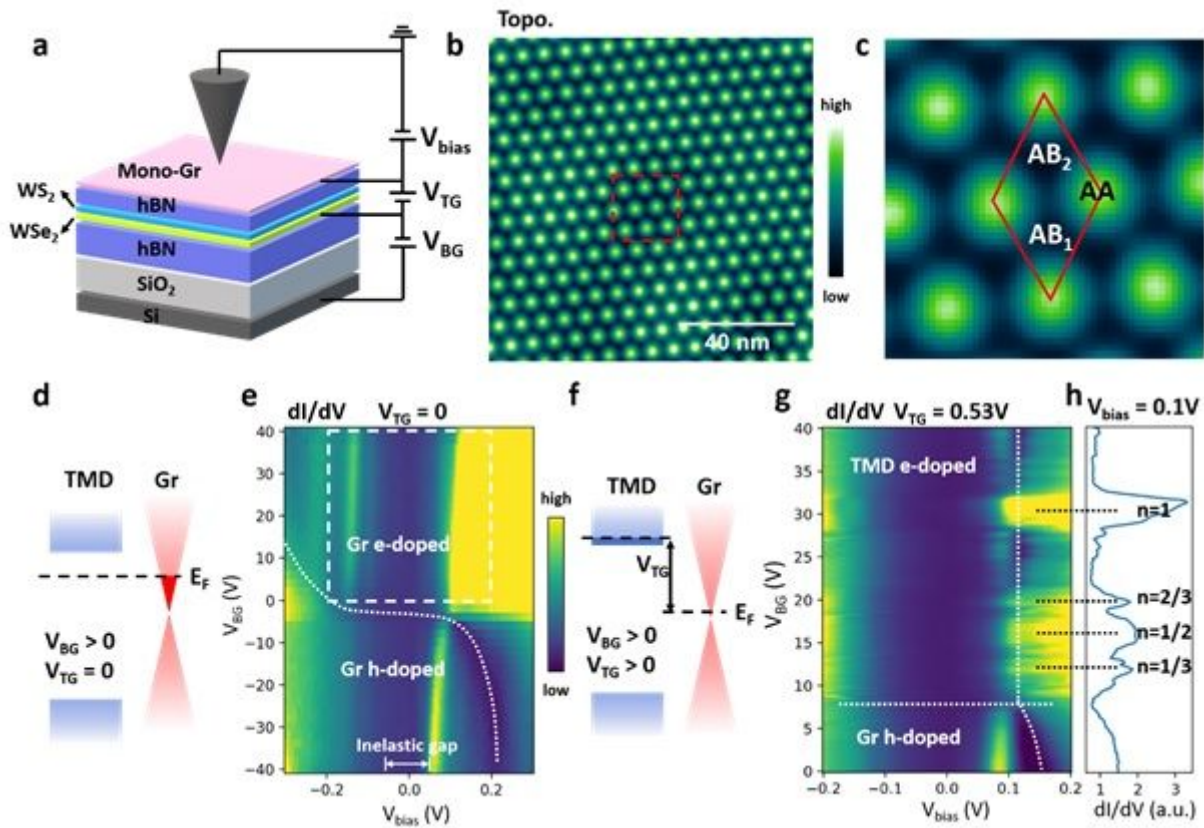


**Figure 1**

STM measurement of the Wigner crystal states in a dual-gated WSe<sub>2</sub>/WS<sub>2</sub> moiré superlattice. a. Schematic of the dual-gated WSe<sub>2</sub>/WS<sub>2</sub> moiré heterostructure device. The top hBN thickness (5nm) is slightly smaller than the moiré lattice constant (8nm). Top gate (VTG) and bottom gate (VBG) voltages are applied to control the carrier density in the WSe<sub>2</sub>/WS<sub>2</sub> heterostructure as well as the top graphene sensing layer. b. A typical large-scale topography image measured on the top graphene surface. V<sub>bias</sub> = 180mV and I = 300 pA. c. Zoom-in image of the red dashed box in (b). The red rhombus labels a primitive cell. Peaks correspond to AA stacking regions and the two inequivalent low points correspond to distinct AB stacking regions (denoted as AB<sub>1</sub> and AB<sub>2</sub>). d. Schematic of the heterostructure band alignment and Fermi levels for V-TG = 0 and VBG > 0. At zero VTG, the Fermi level of the WSe<sub>2</sub>/WS<sub>2</sub> heterostructure is located in the band gap. e. VBG-dependent dI/dV spectra measured on graphene at an AA stacking site for VTG = 0. The dispersive feature marked by the white dotted curve shows the evolution of the graphene charge neutral point (CNP) induced by electrostatic doping from VBG. The persistent gap near V<sub>bias</sub> = 0 arises from an inelastic tunneling gap that exists at all gate voltages. Due to this inelastic tunneling gap, the graphene CNP curve shows an abrupt shift as it is stepped over zero bias. The tip height was set by the parameters: V<sub>bias</sub> = -300mV and I = 100 pA. f. Schematic of the heterostructure band alignment and Fermi levels for V-TG > 0 and VBG > 0. Application of an appropriate positive VTG allows the Fermi level of the WSe<sub>2</sub>/WS<sub>2</sub> heterostructure to be lifted into the conduction band edge. g. VBG-dependent dI/dV spectra measured on graphene at an AA stacking site for VTG = 0.53V. This is a zoom-in of the electron doped regime corresponding to the phase space denoted by the white dashed box in e. The graphene is hole-doped in the region below the horizontal dashed line (VBG < 7V), and the WSe<sub>2</sub>/WS<sub>2</sub> is electron-

doped in the region above it ( $V_{BG} > 7V$ ). The vertical white dash curve indicates the the expected movement of the graphene CNP for a non-interacting picture. Significant electron doping of the graphene layer takes place at  $n = 1/3, 1/2, 2/3$ , and 1 (denoted by horizontal black dashed lines in (g)). The tip height was determined by the setpoint:  $V_{bias} = -200mV$  and  $I = 100 pA$ . h. Vertical line-cut of the  $V_{BG}$ -dependent  $dI/dV$  spectra in (g) at  $V_{bias} = 0.1V$  shows peaks at  $n=1, 2/3, 1/2$ , and  $1/3$ .

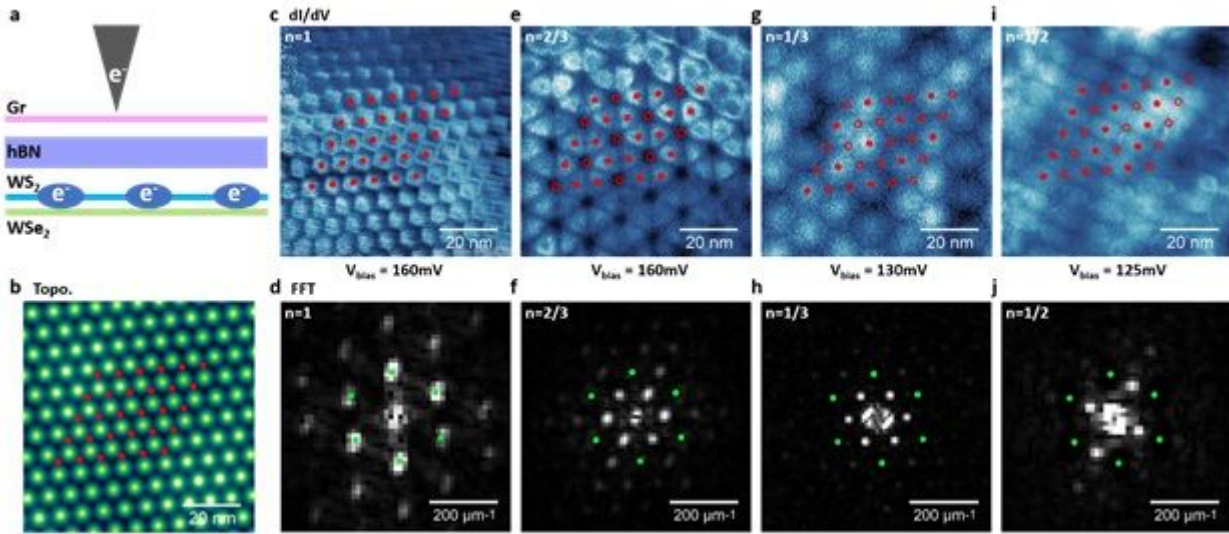


**Figure 2**

Imaging of the Mott and generalized Wigner crystal states. a. Schematic shows imaging of the correlated states at a WSe<sub>2</sub>/WS<sub>2</sub> moiré superlattice beneath a graphene sensing layer.  $dI/dV$  maps are acquired on the top graphene surface. b. a typical topography image of the moiré superlattice shows a perfect lattice without distortion or defects. The triangular lattice formed by the AB1 stacking sites is marked by solid red dots. c.  $dI/dV$  map of the  $n = 1$  Mott insulator ( $V_{bias} = 160mV$ ,  $V_{\rightarrow BG} = 30V$ ,  $VTG_{\rightarrow} = 0.53 V$ ). The triangular lattice formed by the AB1 stacking sites is labeled with red dots. d. Fast Fourier transform (FFT) of the image shown in (c). The reciprocal unit vectors of the moiré superlattice are labeled by green dots. e-j.  $dI/dV$  mappings of the generalized Wigner crystal states for various electron fillings and the corresponding FFT images: e.  $dI/dV$  map of  $n = 2/3$  state ( $V_{bias} = 160mV$ ,  $V_{\rightarrow BG} = 21.8V$ ,  $VTG_{\rightarrow} = 0.458 V$ ). f. FFT of  $n = 2/3$  state shown in (e). g.  $dI/dV$  map of  $n = 1/3$  state ( $V_{bias} = 130mV$ ,  $V_{\rightarrow BG} = 14.9V$ ,  $VTG_{\rightarrow} = 0.458 V$ ). h. FFT of  $n = 1/3$  state shown in (g). i.  $dI/dV$  map of  $n = 1/2$  state ( $V_{bias} = 125mV$ ,  $V_{\rightarrow BG} = 18.7V$ ,  $VTG_{\rightarrow} = 0.458 V$ ). j. FFT of  $n = 1/3$  state shown in (i). FFT filtering was performed in the Wigner crystal images (e-j) to suppress the periodic feature associated with the moiré superlattice (i.e. green dots in (f,h,j). see SI for unfiltered images). Electron-filled AB1 sites are labeled with red dots and the empty AB1 sites are labeled with red circles in the real-space images (e,g,i). The reciprocal unit vectors of the moiré superlattice are labeled with green dots in the corresponding FFT images (f,h,j).

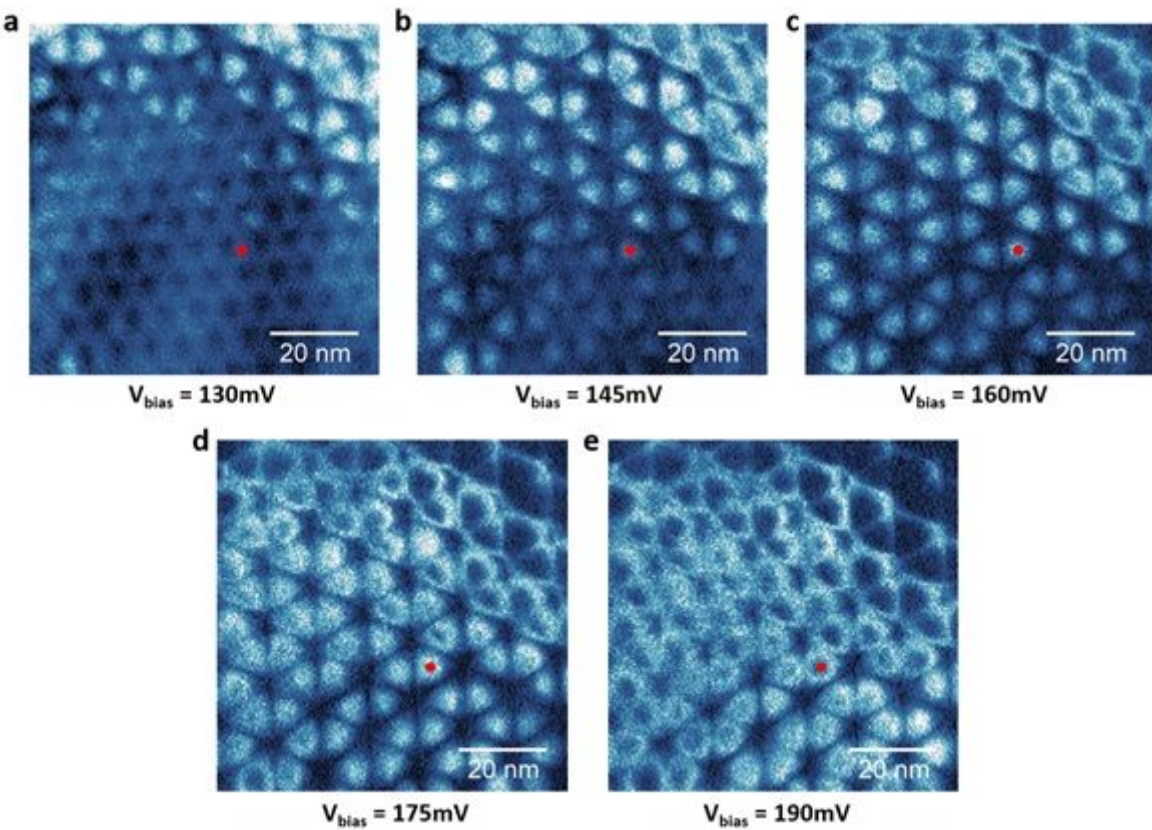


**Figure 3**

Evolution of  $dI/dV$  maps for the  $n = 2/3$  state with increased  $V_{bias}$ . a-e  $dI/dV$  maps of the  $n = 2/3$  generalized Wigner crystal state measured at (a)  $V_{bias} = 130\text{mV}$ , (b)  $V_{bias} = 145\text{mV}$ , (c)  $V_{bias} = 160\text{mV}$ , (d)  $V_{bias} = 175\text{mV}$ , and (e)  $V_{bias} = 190\text{mV}$ . Gate voltage parameters:  $V_{BG} = 21.8\text{V}$ ,  $VTG = 0.458\text{ V}$ . All five maps are measured in the same region and no filtering has been performed. The map in (c) ( $V_{bias} = 160\text{mV}$ ) shows the same data as Fig. 2e, but with no filtering. The red dot labels one typical electron-filled AB1 site where a discharging ring can be observed that get larger with increased  $V_{bias}$  (a common characteristic of discharging phenomena).

## Supplementary Files

This is a list of supplementary files associated with this preprint. Click to download.

- SI43.docx